JACS
JOURNAL OF THE AMERICAN CHEMICAL SOCIETY
Article
Cite This: J. Am. Chem. Soc. 2018, 140, 9261−9268
pubs.acs.org/JACS

Multistates and Polyamorphism in Phase-Change $K_2Sb_8Se_{13}$

Saiful M. Islam,[†] Lintao Peng,[‡] Li Zeng,[‡] Christos D. Malliakas,[†] Duck Young Chung,[§] D. Bruce Buchholz,[∥] Thomas Chasapis,[†] Ran Li,[∥] Konstantinos Chrissafis,[⊥] Julia E. Medvedeva,[#] Giancarlo G. Trimarchi,[¶] Matthew Grayson,[‡,△] Tobin J. Marks,[†,‡,∥] Michael J. Bedzyk,[‡,∥,¶] Robert P. H. Chang,[∥] Vinayak P. Dravid,[∥] and Mercouri G. Kanatzidis*[,†,§]

[†]Department of Chemistry, Northwestern University, Evanston, Illinois 60208, United States
[‡]Applied Physics Graduate Program, Northwestern University, Evanston, Illinois 60208, United States
[§]Materials Science Division, Argonne National Laboratory, Argonne, Illinois 60439, United States
[∥]Department of Material Science and Engineering, Northwestern University, Evanston, Illinois 60208, United States
[⊥]Department of Physics, Aristotle University of Thessaloniki, Thessaloniki, Greece
[#]Department of Physics, Missouri University of Science and Technology, Rolla, Missouri 65409-0640, United States
[¶]Department of Physics and Astronomy, Northwestern University, Evanston, Illinois 60208, United States
[△]Department of Electrical Engineering and Computer Science, Northwestern University, Evanston, Illinois 60208, United States

Supporting Information

ABSTRACT: The phase-change (PC) materials in the majority of optical data storage media in use today exhibit a fast, reversible crystal → amorphous phase transition that allows them to be switched between on (1) and off (0) binary states. Solid-state inorganic materials with this property are relatively common, but those exhibiting an amorphous → amorphous transition called *polyamorphism* are exceptionally rare. $K_2Sb_8Se_{13}$ (KSS) reported here is the first example of a material that has both amorphous → amorphous polyamorphic transition and amorphous → crystal transition at easily accessible temperatures (227 and 263 °C, respectively). The transitions are associated with the atomic coordinative preferences of the atoms, and all three states of $K_2Sb_8Se_{13}$ are stable in air at 25 °C and 1 atm. All three states of $K_2Sb_8Se_{13}$ exhibit distinct optical bandgaps, E_g = 1.25, 1.0, and 0.74 eV, for the amorphous-II, amorphous-I, and crystalline versions, respectively. The room-temperature electrical conductivity increases by more than 2 orders of magnitude from amorphous-I to -II and by another 2 orders of magnitude from amorphous-II to the crystalline state. This extraordinary behavior suggests that a new class of materials exist which could provide multistate level systems to enable higher-order computing logic circuits, reconfigurable logic devices, and optical switches.

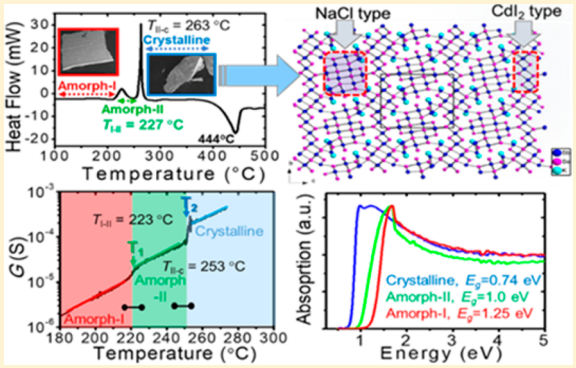

INTRODUCTION

Phase-change (PC) materials are a distinctive class of compounds which can be reversibly and rapidly transformed between an amorphous and a crystalline state. Different atomic arrangements in their amorphous and crystalline phases induce changes in macroscopic properties such as density, optical reflectivity, and electrical resistivity.[1−4] This class of materials is technologically important for nonvolatile read−write optical and electrical storage phase change memory (PCM) hierarchy, particularly in digital versatile disc random access memory (DVD-RAM), digital versatile disc rerecordable (DVD-RW) and Blu-ray disc rewritable (BD-RE), and nonvolatile computer memory such as PC random access memory (PC-RAM) and smart phone technologies.[2,3,5,6]

In the 1950s, Ovshinsky investigated the electronic properties of disordered semiconductors and discovered two reversible switching phenomena of electrical resistivity, known as ovonic threshold switching (OTS) and ovonic memory switching (OMS).[7] Since then, OTS and OMS have been observed in many materials such as nickel oxide,[8] amorphous silicon,[9] metal−semiconductor,[10] and chalcogenides,[7] thus driving efforts to exploit these properties for applications in electronic memory.[11] Among these materials, chalcogenides such as GeTe, Ge_4SbTe_5, $Ge_2Sb_2Te_5$, Sn2Se3, In_2Se_3, In_3SbTe_2, $Ag_4In_3Sb_{12}Te_{26}$, and $Ag_{3.5}In_{3.8}Sb_{75}Te_{17.7}$ have been a subject of intense study;[4,12−15] however, only a few of them, such as $Ge_2Sb_2Te_5$ (GST) and Ag- and In-doped antimony telluride (collectively known as AIST), have proven suitable for use in high-density data storage and high speed

Received: May 26, 2018
Published: June 29, 2018

DOI: 10.1021/jacs.8b05542
J. Am. Chem. Soc. 2018, 140, 9261−9268

cognitive computing.[2,4,16,17] The ideal candidate should also exhibit stable resistivity in the amorphous state, so as to enable devices of multilevel storage via multibit cells—an emerging technology for high density data storage using PCM cells.[16−18] Apart from this class of p-block metal chalcogenides, a stoichiometric, wide band gap material, KSb_5S_8, has been reported, but its slow crystallization rate hinders its practical use in PCM technology.[19,20]

Charge Transport. Flakes with dimensions of ∼5*5*0.120 mm3 were used for the transport experiment. Standard dc techniques (Keithley 4200) were used to measure the van der Pauw four-point resistivity of the $K_2Sb_8Se_{13}$ sample inside a rapid-thermal-annealing oven with electrical feedthroughs. The sample flake and measurement thermometer were mounted onto a glass substrate with high-temperature carbon paste. The glass substrate was then placed on a tungsten heater filament which was fed with a high current, and sample resistance was correlated with filament temperature. For annealing cycle measurements, the sample conductivity was measured at room temperature after cycling to the temperature T_{Anneal}. The oven was pumped to vacuum for all the experiments.

Polyamorphism on the other hand is a phase-change phenomenon that is found in some binary compounds (e.g., SiO_2, GeO_2, GeS_2, BeF_2) and single elements (C, Ge, Bi, Se, Te, P, I) under very high pressures. Pressure-dependent polyamorphism has been observed for the GaSb and $GeSb_2Te_4$ alloys.[21,22] Based on the crystallization kinetics, polyamorphism was also predicted for the Ga-Sb alloys ($Ga_{14}Sb_{86}$ and $Ga_{46}Sb_{54}$). The slower kinetics was obtained for films grown by DC magnetron sputtering, while higher kinetics was obtained for the laser-remelted films, suggesting growth-dependent polyamorphism.[21] Polyamorphism at room pressure is quite rare.[23−27] Ashland et al. reported that the supercooled state of Al_2O−-Y_2O_3 exhibits the coexistence of two glassy liquids with the same composition; however, their densities are different.[28] This finding indicates that even a single-component liquid phase can separate into two liquid phases. Such a transition in the liquid state still seems controversial. This situation partly derives from the counterintuitive nature of the phenomena and experimental difficulties. For example, in most cases the transition tends to be at high temperatures or pressures or masked by other events such as solidification, e.g., for water. Tanaka presented a general view of an amorphous−amorphous phase transition, based on a simple physical picture that there is "cooperative medium-range bond ordering" in such materials.[29] Contrary to general belief, he argued that amorphous materials are not homogeneous, but they possess locally favored structures. In the case of $K_2Sb_8Se_{13}$ our experimental data support this proposal.

Here we report the remarkable behavior of $K_2Sb_8Se_{13}$ (KSS), a new ternary chalcogenide that shows a unique "amorphous to amorphous", polyamorphic phase change at ambient pressure. In addition, it also exhibits the classical "amorphous to crystal" transition, making it a unique three-state PC system. KSS can be grown as a single-phase thin film with a well-defined crystal structure containing both ionic and covalent bonding interactions. Each of the states exhibits a distinctly different optical bandgap and electrical resistivity. This material represents the first example of a stoichiometric polyamorphic material operational at room pressure.

EXPERIMENTAL SECTION

Synthesis. Crystalline $K_2Sb_8Se_{13}$ was synthesized by combining 0.345 g of K_2Se, 1.948 g of Sb, and 1.895 g of Se powders under a nitrogen atmosphere in a 13 mm diameter, fused silica tube, which was then sealed under a pressure of $<10^{-4}$ torr and heated at 850 °C for 24 h. When heating was complete, the tube was allowed to cool in the furnace. The resulting ingot was proven to have the $K_2Sb_8Se_{13}$ stoichiometry by energy-dispersive X-ray elemental analysis (EDS) and powder X-ray powder diffraction (PXRD). The ingot was pulverized and placed inside a 9 mm fused silica half tube (one end was a sealed tube). Working inside a nitrogen atmosphere glovebox the tube containing the melt was poured over two counter rotating copper cylinders. Each copper cylinder was 2 in. in diameter. The melt was poured very fast just by flipping the tube over the rotating cylinder. This process gave thin glassy flakes of ∼110−130 μm thick. Glass formation was confirmed by X-ray powder diffraction, and thermal events were studied with a Shimadzu DSC-50 differential scanning calorimeter. Synchrotron radiation scattering studies were carried out at the Advanced Photon Source at Argonne National Laboratory.

X-ray Single-Crystal Diffraction. A single crystal with dimensions 0.666 × 0.034 × 0.024 mm^3 of $K_2Sb_8Se_{13}$ was mounted on the tip of a glass fiber. Intensity X-ray diffraction data were collected at 293 K on a Bruker SMART Platform CCD diffractometer using graphite-monochromatized Mo Kα radiation over a full sphere of reciprocal space, up to 60.2° in 2θ. The individual frames were measured with an omega rotation of 0.3° and an acquisition time of 60 s. The unit cell axes were confirmed by zone (*hk*0 and *h*0*l*) photos after data collection. The SMART software was used for the data acquisition and SAINT for data extraction and reduction.[30] The analytical absorption correction was applied, and the structure solution and refinement (full-matrix least-squares on F^2) were done with the SHELXTL/SHELX97 package of crystallographic programs. The structure was solved with the direct method, and all atoms were refined anisotropically. Detailed crystallographic data have been reported in in the Supporting Information, Tables S1−S3.

Pair Distribution Function (PDF) Analysis. The local structure was solved using atomic pair distribution function (PDF) analysis. Powder from crystalline and amorphous $K_2Sb_8Se_{13}$ samples was packed onto a flat aluminum plate to a thickness of 1.0 mm and sealed with kapton tape. Diffraction data were collected at 300 K using the rapid acquisition pair distribution function (RA-PDF) technique.[31] Data were collected using an MAR345 image plate detector and ∼100 keV energy X-rays (λ = 0.123515 Å) at the 6-IDD beam line at the Advanced Photon Source (APS). Measurements were repeated 4−5 times per sample to improve counting statistics. The data were combined and integrated using the program FIT2D.[32] Corrections were made for background subtraction, Compton effect and fluorescence scattering, geometric corrections, absorption, and so on, as described in reference 33. The corrections were made using PDFgetX2.[34] Finally, $S(Q)$ was truncated at Q_{max} of 25 $Å^{-1}$ before the PDF was calculated. Structural models are fit to the data using the program PDFFIT.[35]

Optical Energy Band Gaps. Optical diffuse reflectance measurement was carried out on finely ground samples at room temperature. The spectrum was recorded, in the UV−vis−NIR region 300−2500 nm, with the use of an UV-3600 Shimadzu UV-3600 PC double-beam, double-monochromator spectrophotometer. A background was collected before each scan using $BaSO_4$. Absorption (α/S) data were calculated from the reflectance data using the Kubelka−Munk equation: $\alpha/S = (1 - R)^2/2R$, where R is reflectance; α is the absorption coefficient; and S is the scattering coefficient.[36] The absorption edge was estimated by linearly fitting the absorbance of the converted data.

Pycnometry. Density was calculated from the sample mass (∼40−60 mg) and the volume determined from a Micromeritics AccuPyc 1340 gas pycnometer at 293 K. Samples of amorphous-II were obtained by heating amorphous-I to 230 °C in a Shimadzu DSC-50 and rapidly cooling to obtain the desired glassy phase.

DOI: 10.1021/jacs.8b05542
J. Am. Chem. Soc. 2018, 140, 9261−9268

Transmission Electron Microscopy. Bright-field transmission electron microscopy was conducted using a TEM HT 7700 under 60 kV acceleration voltage. Diffraction patterns were captured by selecting a thin area on the bright-field image. The TEM sample was prepared by cryogrinding with liquid nitrogen for more than 2 h to thin the samples enough for imaging.

Film Growth. Thin-film $K_2Sb_8Se_{12}$ specimens were grown by pulsed-laser deposition (PLD) at Northwestern University using a spark plasma sintering pellet as a target. The SPS condition was 623 K for 5 min under an axial pressure of 40 MPa. A round pellet, with 14 mm diameter and 3 mm thickness, was obtained with mass density over ~90% of the theoretical value. The surfaces of the pellet were polished in order to remove graphite layers as well as to smooth the surface. PLD was accomplished with a 248 nm KrF excimer laser, 25 ns pulse duration, and 2 Hz repetition rate. The 200 mJ/pulse beam was focused to a 1 mm × 2 mm spot size. The target was rotated at 5 rpm about its axis to prevent localized heating. The target−substrate separation was fixed at 8 cm. The films were grown on fused quartz and silicon substrates at the background base pressure, 5×10^{-7} Torr. The films were grown at room temperature. The optical transparency and reflectivity were measured between 250 and 2400 nm with a Perkin-Elmer Lambda 1050 fitted with a 150 mm integrating sphere that was used for both transmission and reflection measurements, in the dual-beam mode. The transmittance (T), reflectance (R), absorption coefficient (α: 1/cm), and optical band gap (E_g: eV) were then calculated.

In Situ Grazing-Incident Wide-Angle X-ray Scattering (GIWAXS) Experiments. GIWAXS experiments were performed at sector 5BMC (DuPont-Northwestern-Dow Collaboration Access Team (DND-CAT)) at Advanced Photon Sources with incident X-ray energy 20 keV and the critical angle of Si is ~0.09 degree. PLD-deposited $K_2Sb_8Se_{13}$ thin film was placed in a Beryllium dome mini chamber and annealed under vacuum conditions with a 0.2 °C/min ramping rate. A MarCCD (165 mm in diameter) area detector was used to monitor the amorphous to crystalline transition and collect time-sequenced diffraction patterns. The raw 2D images were processed by using Nika software. Two representative images were selected to show diffraction patterns for both the amorphous phase and crystalline phases. We measured the GIWAXS patterns of amorphous $K_2Sb_8Se_{13}$ (KSS) before and after we put on the Be dome. The bright and scattered points at the high Q regions are originated from the beryllium dome. Those peaks only showed up with the Be dome, so we attribute the diffraction peaks in the amorphous sample to the Be dome, and the location of the peaks did not change throughout the experiment, also confirming this phenomenon. The incident X-rays interact with the front of the Be dome before reaching the sample surface, and the scattered X-rays from the sample interact with the back of the Be dome. It is important to mention that there are actually two possible scattering events that could contribute to the observation of Be dome diffraction peaks: The incident X-rays interact with the front of the Be dome before reaching the sample surface, and the scattered X-rays from the sample interact with the back of Be dome. However, the former event should result in the higher intensities and larger q values of diffraction peaks than the latter. So, these peaks are not due to the multiple scattering of diffraction off the crystalline KSS materials. Time-sequenced 1D diffraction patterns were generated by circular averaging the diffraction rings.

Band Structure Calculations. In order to investigate the electronic structure of crystalline $K_2Sb_8Se_{13}$, first-principles calculations were carried out within the density functional theory formalism using the Projector-Augmented Wave method[37] implemented in the Vienna Ab-initio Simulation Package.[38,39] The energy cut off for the planewave basis was set to 360 eV. The generalized gradient approximation (GGA), a functional of Perdew−Burke−Ernzerhof (PBE),[40] was employed. The crystal structures and the lattice parameters were fixed to their experimentally observed values, but the positions of atoms in the cells were relaxed until the atomic forces on each atom were less than 0.01 eV/Å. The Monkhorst−Pack k-point grids of 4 × 8 × 4 were used for Brillouin zone (BZ) sampling for $K_2Sb_8Se_{13}$. The electronic and optical properties of triclinic $K_2Sb_8Se_{13}$ (space group P-1 with 4 f.u.) and of the amorphous $K_2Sb_8Se_{13}$ structures were calculated. To overcome the failure of the generalized gradient approximation to correctly predict band gaps of semiconductors, the exchange and correlation effects were treated using the hybrid Heyd−Scuseria−Ernzerhof (HSE06) approach[41,42] with a mixing parameter of 0.25 and a screening parameter μ of 0.2 $Å^{-1}$.

Ab Initio Molecular Dynamics Simulations and DFT Calculations. Amorphous $K_2Sb_8Se_{13}$ structures were generated using first-principles molecular dynamics (MD) liquid-quench simulations as implemented in the Vienna Ab Initio Simulation package (VASP).[38,39,43] For this, the initial cell of $K_{12}Sb_{48}Se_{78}$ with triclinic structure was melted at 2000 K for 60 ps to remove the crystalline memory. Next, two cubic cells with $K_{12}Sb_{48}Se_{78}$ melt, one with a density of 4.95 g cm^{-3} (corresponds to amorphous-I upon quenching) and another with a density of 5.28 g cm^{-3} (corresponds to amorphous-II upon quenching), were rapidly quenched to 100 K at the rate of 100 K/ps. During melting and quenching processes, a cutoff of 160 eV was used, and the k-point sampling was restricted to Γ-point only. Both structures were then equilibrated at 300 K for 6 ps. All simulations were carried out within the NVT ensemble with a Nose−Hoover thermostat using an integration time step of 2 fs. The two atomic configurations obtained from the ab initio MD simulations were optimized using density functional calculations with generalized gradient approximation using the PBE functional.[40] During the optimization, the 4 × 4 × 4 Γ-centered k-point mesh was used; the atomic positions were relaxed until the Hellmann−Feynman force on each atom was below 0.01 eV/Å. The local structure characteristics, namely, the Sb−Se distance and the Sb−Se effective coordination number distributions, are calculated according to refs.[44,45]

RESULTS AND DISCUSSION

$K_2Sb_8Se_{13}$ was synthesized by cooling a stoichiometric melted mixture of K_2Se, elemental antimony, and elemental selenium. $K_2Sb_8Se_{13}$ crystallizes in a triclinic structure with a three-dimensional framework of distorted octahedral $SbSe_6$ units (Figure 1A). The structure is a variant of β-$K_2Bi_8Se_{13}$[46] and includes two different types of Sb/Se building units which as they assemble form parallel tunnels filled with K^+ atoms (Figure 1A). The complex 3D network of $K_2Sb_8Se_{13}$ consists of NaCl- and CdI_2-type blocks arranged side by side to form arrays perpendicular to the b-axis. Thus, the crystal structure of $K_2Sb_8Se_{13}$ differs from KSb_5S_8, another phase change material that is comprised of infinitive undulating slabs of $[Sb_5S_8]^-$.[19] Thermogravimetric analysis of $K_2Sb_8Se_{13}$ does not show any mass loss up to 773 K, which is beyond its melting point (~717 K) obtained by DSC and will be discussed later.

$K_2Sb_8Se_{13}$ is a p-type semiconductor with a room-temperature Seebeck coefficient of 870 μV/K which decreases slowly to 625 μV/K at 525 K (SI, Figure S1). $K_2Sb_8Se_{13}$ possesses a very low thermal conductivity of ~0.42 W m^{-1} K^{-1} at room temperature which slightly decreases with rising temperatures ranging from RT to 525 K (SI, Figure S1). Such low thermal conductivity could probably be the result of short mean-free-path lengths of the heat-carrying phonons; this in turn may reflect a combined effect of the complexity of the crystal structure as well as of "rattler" activity of the K^+ ions in tunnels.

The bulk crystalline−amorphous transition of $K_2Sb_8Se_{13}$ is achieved by quenching the molten mass of the crystalline phase using a melt spinner (see SI for details and SEM-EDS in Figure S2). Powder X-ray diffraction (PXRD) of the as-synthesized amorphous phase, which we call amorphous-I, reveals three broad features visible at 2θ angles of 13−17°, 23−35°, and 42−58°, indicating a certain degree of atomic organization in the amorphous-I phase, although it clearly has no periodic

DOI: 10.1021/jacs.8b05542
J. Am. Chem. Soc. 2018, 140, 9261−9268

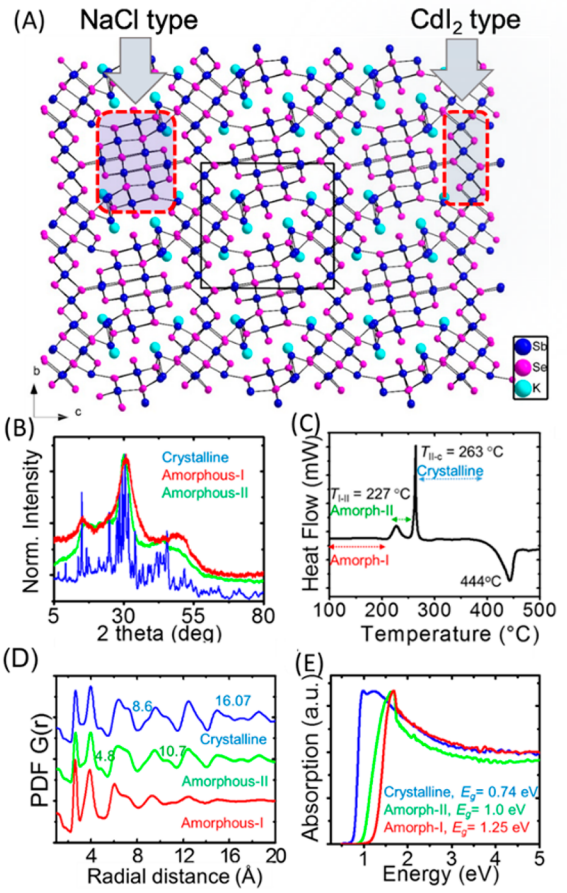

Figure 1. (A) Crystal structure of $K_2Sb_8Se_{13}$ [triclinic P-1, Z = 4, a = 8.1854(8) Å, b = 17.7397(17) Å, c = 18.5286(18) Å, α = 90.188(2)°, β = 90.180(2)°, and γ = 103.271(2)°]. (B) PXRD of the crystalline (blue), amorphous-I (red), and amorphous-II (green) phase. (C) On heating the as-grown amorphous phase DSC shows two exothermic peaks at $T_{I\text{-}II}$ = 227 °C and $T_{II\text{-}c}$ = 263 °C, characteristic for amorphous-I to amorphous-II and amorphous-II to crystalline transitions. (D) and (E) PDF and UV/vis absorption patterns of crystalline (blue), amorphous-I (red), and amorphous-II (green) phases.

structure (Figure 1B; amorphous-I). Upon heating, the material undergoes two, well-defined, exothermic transitions, as evidenced in differential scanning calorimetry (DSC, Figure 1C). The first transition from the amorphous-I phase, beginning at $T_{I\text{-}II}^{bulk}$ = 227 °C, represents reorganization to another amorphous structure, which we name amorphous-II. X-ray diffraction data reveal the amorphous nature of this sample (Figure 1B; amorphous-II); however, there are clearly some changes in structure as suggested by the considerable sharpening of broad peaks in the range 23−35°. With further heating to $T_{II\text{-}c}^{bulk}$ = 263 °C, we observe another exothermic reorganization, this time to a crystalline product (Figure 1B; crystalline). In the PXRD pattern of Figure 1B all peaks of the $K_2Sb_8Se_{13}$ structure are observed and no amorphous background. The exothermic nature of the two transitions suggests the amorphous-I and amorphous-II phases are metastable. Transmission electron microscopy (TEM) shows no evidence of nanocrystallites in either the amorphous-I or amorphous-II phases (Figure S3).

To better understand the evolution of the local structure in these amorphous samples we used pair-distribution function (PDF) analysis (Figure 1D). In the as-synthesized amorphous-I (Figure 1D; red spectrum), the presence of atomic pair correlations indicates local bond ordering to nearly 10 Å, a considerable distance for a glassy material. There are clear peaks at ∼2.6 Å, showing Sb−Se bonds, and at ∼4 Å and 6.5 Å, showing second (Se···Se and Sb···Sb) and third nearest-neighbor distances. On conversion to amorphous-II (Figure 1D; green spectrum) additional peaks develop at 4.9 Å, 7.1 Å, 10.7 Å, and 12.4 Å, showing that the transition from the amorphous-I to amorphous-II phase indeed leads to a change in the local and medium-range structure and that this new structure is more ordered than in amorphous-I but not yet periodic. The PDF of the crystallized sample (Figure 1D; blue spectrum) shows the much larger crystallite sizes with better defined correlation peaks, as well as new correlation peaks at much longer radial distances, consistent with full crystallization of the framework. The density data show a slight increase in density upon transition from amorphous-I (ρ_I = 4.949(1) g/cm^3) → amorphous-II (ρ_{II} = 5.060(1) g/cm^3), an increase by $\Delta\rho/\rho_I$ ∼ 2.43%, and then a biggest increase to ρ = 5.278(1) g/

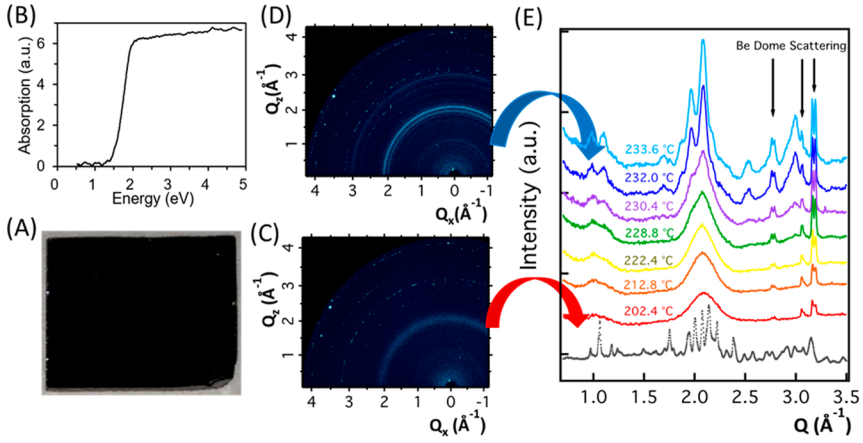

Figure 2. (A) Thin film (∼20 nm thickness) of $K_2Sb_8Se_{13}$ was grown on silica substrate by PLD; (B) optical bandgap energy, thin film $E_{g,I}^{film}$ ∼ 1.5 eV obtained by transmission spectroscopy; and (C) and (D) 2D diffraction images of the as-grown amorphous KSS and after-annealed crystalline KSS. (E) Time-sequenced 1D diffraction patterns color coated with temperatures labeled. The bottom gray curve is an X-ray diffraction pattern of the powder crystalline KSS sample. The diffraction peaks at the Q region between 3.0 and 3.5 (Å^{-1}) as indicated by downward arrows are scattering from the Be dome minichamber. In situ GIWAXS shows that KSS transforms from the amorphous to crystalline phase at ∼232 °C.

DOI: 10.1021/jacs.8b05542
J. Am. Chem. Soc. 2018, 140, 9261−9268

cm^3, corresponding to $\Delta\rho/\rho_{II} \sim 4.5\%$ (see SI for measurement details), in agreement with the PXRD and PDF results. Furthermore, UV/vis absorption spectroscopy also validates the tristability of the KSS (Figure 1E). The shifting of the band gap from E_g = 1.25 to 1.00 to 0.74 eV tracks the switching from amorphous-I → amorphous-II → crystalline phase, respectively.

In general, amorphous semiconductors tend to have optical states called "tail states" that extend from the band edges into the bandgap. These states arise from disorder and a variety of defects.[47] In contrast to this general phenomenon, for KSS, the massive, near doubling of the bandgap, $E_g \sim 0.74 \rightarrow 1.25$ eV, in the opposite direction must be attributed to a major modification in electronic structure in its crystalline and amorphous state transition. This type of bandgap opening is also observed in the case of GST, which increases from $E_g \sim$ 0.50 to 0.7 eV on transition from its crystalline to amorphous versions.[48] Kolobov et al.[6] reported that this blue shift in band gap energy of GST was attributed to changes in coordination number (CN) and geometry, arising from the germanium coordination transition from octahedral to tetrahedral coordination in the crystalline to amorphous phase; however, this atomistic model is no longer the most plausible explanation as other authors[49,50] showed that the transition is due to a decrease of an octahedral distortion upon crystallization. In KSS we presume that the substantial drop in bandgap energy from the amorphous-I ($E_{g,I}^{bulk}$ = 1.25 eV) to the amorphous-II ($E_{g,II}^{bulk}$ = 1.00 eV) and to the crystalline phase ($E_{g,c}^{bulk}$ = 0.74 eV) is plausibly the result of a dramatic change in the number of bonds and in the local order. These can induce significant changes in orbital overalp which in turn can result in the marked optical contrast among the amorphous-I, amorphous-II, and crystalline states. Further details will be discussed later in the light of an *ab initio* molecular dynamics simulation.

KSS films, ~20 nm thick, were grown by pulsed-laser deposition (PLD) on silicon substrates (Figure 2A) (for details see Experimental Section). Grazing-incident wide-angle X-ray scattering (GIWAXS) was employed to study the amorphous to crystalline transition of PLD-grown KSS film, and an area detector was used to collect 2D diffraction images (examples Figures 2C and D). Time-sequenced 1D diffraction patterns were then subsequently generated by circular averaging the diffraction images. In Figure 2C, a broad amorphous ring is observed indicating the as-grown film is amorphous. *In situ* GIWAXS results show that the KSS thin film transforms from an amorphous to crystalline phase at ~232 °C (Figure 2E), a lower temperature than the KSS bulk. Such deviations of the crystallization temperature of the amorphous film relative to bulk KSS ($T_{II\text{-}c}^{bulk} \sim 263$ °C) may reflect the nanoscale film thickness. In addition, the role of different growth mechanisms, morphologies, or surface-to-volume ratios cannot be completely ruled out. Optical transmission spectra show that the as-grown amorphous films exhibit a bandgap, E_g = 1.5 eV, which is larger than that of the bulk powder of amorphous flakes which were grown by melt spinning.

Electrical transport measurement on KSS-exfoliated bulk flakes (see SI for flake synthesis and transport measurement details) likewise reveals evidence of two phase transitions in $K_2Sb_8Se_{13}$. The temperature-dependent conductance curve in Figure 3A shows sharp resistivity increases at temperatures of T_1 = 223 °C and T_2 = 253 °C which can be identified as electrical transport signatures of the phase transition from

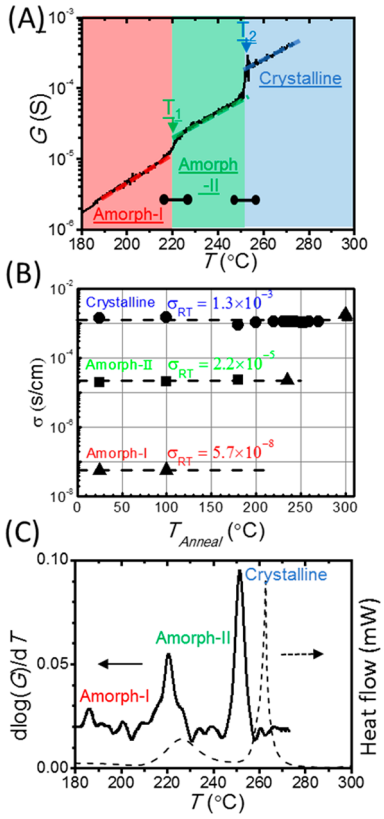

Figure 3. (A) Conductance G vs temperature T on heating the as-grown amorphous phase. The conductance of each phase increases exponentially as the temperature increases. Two-step features are observed at T_1 = 223 °C and T_2 = 253 °C which are slightly lower than the two phase transition temperatures observed in the DSC experiment. The horizontal error bar crossing the phase border indicates the fwhm of phase transition peak in DSC experiment. Dashed tangent lines indicate the conductance increases by 2× and 3× at T_1 and T_2, respectively, which are strong evidence of a phase transition. (B) Room-temperature conductivity σ vs annealing temperature T_{Anneal}. The initial phase of each device before the anneal-cycle experiment shown here is amorphous-I (Triangle), amorphous-II (Square), and crystal (Round). Dashed lines are guide to the eyes. The room-temperature conductivity of each phase increases by orders of magnitude. The room-temperature conductivity is quite consistent for the amorphous-I phase for anneal temperatures $T_{anneal} < T_{I\text{-}II}$; for the amorphous-II phase for anneal temperatures $T_{I\text{-}II} < T_{anneal} < T_{II\text{-}c}$; and for the crystalline phase for anneal temperatures $T_{II\text{-}c} < T_{anneal}$, indicative of a stable phase change. (C) Derivative of log(G) vs temperature T; solid lines and stretched lines represent DSC upon heating of the pristine amorphous KSS phase.

amorphous-I to -II and amorphous-II to crystal, respectively. The transition temperatures determined by the transport experiments are shifted several degrees lower than the bulk transitions determined by DSC measurements mentioned above, $T_{I\text{-}II}^{bulk}$ = 227 °C and $T_{II\text{-}c}^{bulk}$ = 263 °C. Although the temperature shift may be due to minor measurement discrepancies and sample variations, the relative positions of the two peaks and their relative linewidths and peak heights makes a compelling case that they are both signatures of the same phase transitions as observed by DSC.

The room-temperature conductivity of each phase increases by orders of magnitude and remains stable under further low-T annealing as shown in Figure 3B. Three thin flakes (diameter, ~120 μm) with initial amorphous-I (triangle), amorphous-II

DOI: 10.1021/jacs.8b05542
J. Am. Chem. Soc. 2018, 140, 9261−9268

(square), and crystal phases (round) were measured to characterize the room-temperature conductivity of each phase and its stability under a further low-T annealing cycle. The amorphous-I (triangle) phase was annealed in stepwise manner up to 300 °C to cover the conductivity changes of the three phases and is consistent with results from two other flakes. The room-temperature conductivity increases by more than 2 orders of magnitude from amorphous-I to -II and by another 2 orders of magnitude from amorphous-II to the crystalline state (Figure 3C). The stability of the conductivity in each phase under further annealing attests to the robustness of the phase transition and confirms the three-phase nature of $K_2Sb_8Se_{13}$ from an electrical transport perspective.

The nature of the semiconducting character and electronic transitions in crystalline KSS was investigated using electronic band structure calculations (Figure 4A). With the standard generalized gradient approximation (GGA) to the exchange-correlation (XC) functional we predict that the band gap is indirect with a value of $E_{g,c}^{GGA}$ = 0.5 eV, which underestimates the experimental value $E_{g,c}^{bulk}$ = 0.74 eV. The underestimation of the calculated bandgap compared to the experimentally obtained value is a well-known tendency of semilocal XC functionals such as GGA. Using the hybrid functional method in the Heyd−Scuseria−Ernzerhof (HSE) formulation (see Figure 4A), we predict that band gap is $E_{g,c}^{HSE}$ = 0.7 eV in close agreement with the experimental value. From the analysis of the orbital character of the electron states we find that the valence band maximum originates mostly from Se p orbitals, while the conduction band minimum originates mostly from the Sb p orbitals with a Se p component as well.

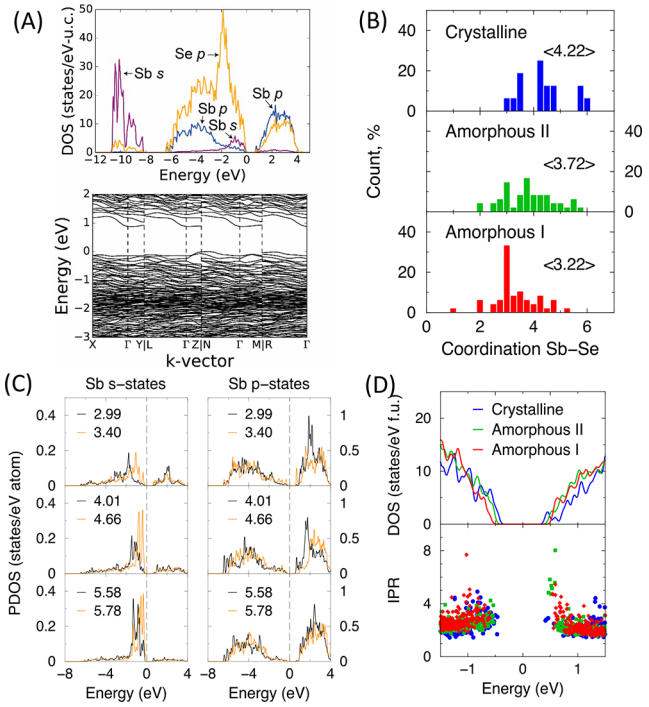

Figure 4. (A) Electronic band structure and density of states of crystalline $K_2Sb_8Se_{13}$.The partial density of states in crystalline $K_2Sb_8Se_{13}$ calculated within density functional theory using the hybrid functional. (B) The distribution of the Sb−Se coordination numbers in crystalline and amorphous-I and -II $K_2Sb_8Se_{13}$ structures obtained from *ab initio* MD simulations. For each structure, the average Sb−Se coordination numbers are shown in brackets. (C) Partial density of states for Sb atoms with different coordination numbers (from 2.99 to 5.78) in crystalline; the Sb s-states (p-states) are given in the left (right) panel, respectively. The Fermi level is at 0.0 eV. (D) Total density of states (DOS) and inverse participation ratio (IPR) calculated for crystalline and amorphous $K_2Sb_8Se_{13}$ structures within density functional theory using hybrid functional. The Fermi level is at 0.0 eV.

To better understand the observed changes in the structural and optical properties of polyamorphic KSS, further theoretical investigations were performed as follows. First, *ab initio* molecular dynamics was employed to determine the local structure of the two amorphous KSS phases with different densities (see Experimental Section for details of the simulations). Figure 4B shows the calculated distribution of Sb−Se distances and the Sb−Se coordination numbers in the three $K_2Sb_8Se_{13}$ structures considered. In agreement with our experimental observations, the calculated Sb−Se first-shell peak in the distribution function broadens upon the transition from the amorphous-I to amorphous-II to crystalline phases (Figure S4A). The observed and calculated trends in the Sb−Se distribution in the three phases show excellent agreement between the experimental and theoretical results as shown in Figure S4: The first peak in the distribution becomes narrower, and the occurrence of the Sb−Se distances within 2.9−3.3 Å is suppressed as we go from crystalline to amorphous-II to amorphous-I. Apart from this, analysis of the local structure reveals that the Sb−Se coordination numbers (CN) change dramatically upon the amorphous-I − amorphous-II transition: while, as expected, amorphous-I corresponds to a statistical distribution of the Sb−Se coordination numbers found in the crystalline $K_2Sb_8Se_{13}$, the number of high-coordinate (CN > 5) Sb atoms is nearly suppressed in amorphous-II which possesses primarily 3-coordinated Sb atoms. As a result, the average Sb−Se CN decreases from 4.2 to 3.7 to 3.2 upon the transition from crystalline to amorphous-II to amorphous-I, respectively. Owing to the covalent nature of the Sb−Se interactions, the Sb coordination with Se atoms determines the resulting electronic properties.

To illustrate the differences in the electronic properties, the calculated partial density of states for the s- and p-orbitals of the Sb atoms with different CNs is plotted in Figure 4C. The results reveal that the s-states of the low-coordinate Sb atoms (CN = 2.99) are broader and located deeper in the valence band versus the s-states of the Sb atoms with higher coordination. As the Sb coordination number increases, the Sb s-states gradually shift closer to the valence band maximum, becoming more localized and fully occupied. Note here that the Sb p-states near the band edges, on the other hand, show little variation with the Sb coordination (Figure 4C). Finally, the electronic properties of the crystalline and amorphous $K_2Sb_8Se_{13}$ structures are calculated using the density-functional approach with a hybrid functional and are compared in Figure 4D. The total density of states clearly illustrates an increase in the bandgap upon the transition from the crystalline to amorphous-II and to amorphous-I $K_2Sb_8Se_{13}$ phases, in excellent agreement with the experimental trend and in accord with the increasing number of highly coordinated Sb atoms. It is important to note that both the experimental observations and theoretical calculations show that the Sb−Se distances vary insignificantly upon the transitions (within only 2% overall)—as evident from the location of the first peak in the observed PDF and in the calculated Sb−Se distance distribution (see Figure S4). Therefore, densification that occurs upon

DOI: 10.1021/jacs.8b05542
J. Am. Chem. Soc. 2018, 140, 9261−9268

crystallization does not affect the local, nearest-neighbor Sb−Se distances and, hence, cannot affect the Sb−Se interactions and, ultimately, the band gap. Instead, our calculations reveal (Figure 4C) that variation in the Sb−Se coordination gives rise to pronounced differences in the valence bandwidth resulting in the band gap differences in the three phases. These allow us to conclude that the electronic structures of Sb−Se states govern the band edges (Figure 4A, C), and thus, the Sb−Se interactions determine the overall electronic and optical properties of the material. The calculated optical band gap values (at Γ point) are 0.86 eV, 1.13 eV, and 1.30 eV, for the crystalline, amorphous-II, and amorphous-I phase, respectively. Note that the calculated band gap in crystalline $K_2Sb_8Se_{13}$ is indirect with the valence band maximum at a *k*-point between the Γ and N points, i.e., along the [101] direction, of the triclinic Brillouin zone and with the conduction band minimum at the Γ point. Importantly, the calculated inverse participation ratio (IPR) for the amorphous $K_2Sb_8Se_{13}$ phases reveals that the top of the valence band is free of strongly localized tail states, whereas the high IPR values near the bottom of the conduction band bottom are due to the formation of Sb−Sb defect states.

CONCLUDING REMARKS

In summary, the novel chalcogenide $K_2Sb_8Se_{13}$ exhibits unique amorphous → amorphous phase transition, *polyamorphism*, besides a conventional crystal → amorphous transition. This tristability of $K_2Sb_8Se_{13}$ occurs at ambient pressure. Each of the phases exhibits sharply contrasting electrical resistivity over 2 orders of magnitude and also optical bandgaps differing by steps of ∼ 0.25 eV at each transition. If the occurrence of polyamosphism is more common than previously thought at standard pressures, we could anticipate future discoveries of such materials with ideal three-state behavior. These will be highly attractive for a variety of new science experiments including technological applications related to higher than binary types of logic.

ASSOCIATED CONTENT

Supporting Information

The Supporting Information is available free of charge on the ACS Publications website at DOI: 10.1021/jacs.8b05542.

CIF file for $K_2Sb_8Se_{13}$ (CIF)

Additional experimental details on powder X-ray diffraction, scanning electron microscopy, thermal conductivity, Seebeck measurement, thermal analysis, and electrical transport measurement and Tables S1−S3 and Figures S1−S4 (PDF)

AUTHOR INFORMATION

Corresponding Author

*m-kanatzidis@northwestern.edu

ORCID

Saiful M. Islam: 0000-0001-8518-1856
Li Zeng: 0000-0001-6390-0370
Christos D. Malliakas: 0000-0003-4416-638X
Tobin J. Marks: 0000-0001-8771-0141
Michael J. Bedzyk: 0000-0002-1026-4558
Vinayak P. Dravid: 0000-0002-6007-3063
Mercouri G. Kanatzidis: 0000-0003-2037-4168

Notes

The authors declare no competing financial interest.

ACKNOWLEDGMENTS

SMI, LP, LZ, DDB, VDP, MG, TJM, MGK, MJB, RL and JEM acknowledge support from the MRSEC program (NSF DMR-1720139) at the Materials Research Center. This work made use of EPIC and Keck II facilities of Northwestern University's NUANCE Center, which have received support from the Soft and Hybrid Nanotechnology Experimental (SHyNE) Resource (NSF ECCS-1542205); the MRSEC program (NSF DMR-1720139) at the Materials Research Center; the International Institute for Nanotechnology (IIN); the Keck Foundation; and the State of Illinois, through the IIN. Work at Argonne National Laboratory for discovery and initial characterization of KSS was supported by the U.S. Department of Energy (DOE), Office of Science, Basic Energy Sciences (BES), under contract no. DE-AC02-06CH11357. GIWAXS data were collected at sector 5BMC at DuPont-Northwestern-Dow Collaboration Access Team (DND-CAT) at Advanced Photon Sources. DND-CAT is supported by E.I. DuPont de Nemours & Co., The Dow Chemical Company, and Northwestern University. We thank Dr. D. Keane from sector 5 for helping with the experimental setup. We thank D. Robinson for help with collecting scattering data at the APS Argonne National Laboratory. MUCAT is supported by the U.S. Department of Energy through Contract No. W-7405-Eng-82 and the APS by Contract No. W-31-109-Eng-38. We thank J. B. Wachter and T. Kyratsi for help in the very early stages of this project. Computational resources were provided by the NSF-supported XSEDE program and by Department of Energy NERSC facilities. G.T. used in this research resources of the National Energy Research Scientific Computing Center (NERSC), a DOE Office of Science User Facility supported by the Office of Science of the US Department of Energy under Contract No. DE-AC02-05CH11231.

REFERENCES

(1) Welnic, W.; Pamungkas, A.; Detemple, R.; Steimer, C.; Blugel, S.; Wuttig, M. *Nat. Mater.* **2006**, *5* (1), 56−62.
(2) Wuttig, M.; Lusebrink, D.; Wamwangi, D.; Welnic, W.; Gillessen, M.; Dronskowski, R. *Nat. Mater.* **2007**, *6* (2), 122−8.
(3) Jedema, F. *Nat. Mater.* **2007**, *6* (2), 90−1.
(4) Raoux, S.; Burr, G. W.; Breitwisch, M. J.; Rettner, C. T.; Chen, Y.-C.; Shelby, R. M.; Salinga, M.; Krebs, D.; Chen, S.-H.; Lung, H.-L.; Lam, C. H. *IBM J. Res. Dev.* **2008**, *52*, 465−479.
(5) Sebastian, A.; Le Gallo, M.; Krebs, D. *Nat. Commun.* **2014**, *5*, 4314.
(6) Kolobov, A. V.; Fons, P.; Frenkel, A. I.; Ankudinov, A. L.; Tominaga, J.; Uruga, T. *Nat. Mater.* **2004**, *3* (10), 703−708.
(7) Ovshinsky, S. R. *Phys. Rev. Lett.* **1968**, *21*, 1450−1453.
(8) Gibbons, J. F.; Beadle, W. E. *Solid-State Electron.* **1964**, *7*, 785−797.
(9) Hajto, J.; Snell, A. J.; Hu, J.; Holmes, A. J.; Owen, A. E.; Rose, M. J.; Gibson, R. A. G. *Philos. Mag. B* **1994**, *69*, 237−251.
(10) Simmons, J. G.; El-Badry, A. *Solid-State Electron.* **1977**, *20*, 955−961.
(11) Neale, R. G.; Aseltine, J. A. *IEEE Trans. Electron Devices* **1973**, *20*, 195−205.
(12) Luckas, J.; Piarristeguy, A.; Bruns, G.; Jost, P.; Grothe, S.; Schmidt, R. M.; Longeaud, C.; Wuttig, M. *J. Appl. Phys.* **2013**, *113*, 023704.
(13) Lencer, D.; Salinga, M.; Grabowski, B.; Hickel, T.; Neugebauer, J.; Wuttig, M. *Nat. Mater.* **2008**, *7* (12), 972−7.

DOI: 10.1021/jacs.8b05542
J. Am. Chem. Soc. 2018, 140, 9261−9268

(14) Shportko, K.; Kremers, S.; Woda, M.; Lencer, D.; Robertson, J.; Wuttig, M. *Nat. Mater.* **2008**, *7* (8), 653−8.
(15) Wang, R. Y.; Caldwell, M. A.; Gnana, R.; Jeyasingh, D.; Aloni, S.; Shelby, R. M.; Wong, H.-S. P.; Milliron, D. J. *J. Appl. Phys.* **2011**, *109*, 113506.
(16) Koelmans, W. W.; Sebastian, A.; Jonnalagadda, V. P.; Krebs, D.; Dellmann, L.; Eleftheriou, E. *Nat. Commun.* **2015**, *6*, 1−7.
(17) Athmanathan, A.; Stanisavljevic, M.; Papandreou, N.; Pozidis, H.; Eleftheriou, E. *IEEE Journal on Emerging and Selected Topics in Circuits and Systems* **2016**, *6* (1), 87−100.
(18) Rao, F.; Ding, K.; Zhou, Y.; Zheng, Y.; Xia, M.; Lv, S.; Song, Z.; Feng, S.; Ronneberger, I.; Mazzarello, R.; Zhang, W.; Ma, E. *Science* **2017**, *358* (6369), 1423−1426.
(19) Kyratsi, T.; Chrissafis, K.; Wachter, J.; Paraskevopoulos, K. M.; Kanatzidis, M. G. *Adv. Mater.* **2003**, *15*, 1428−1431.
(20) Mitzi, D. B.; Raoux, S.; Schrott, A. G.; Copel, M.; Kellock, A.; Jordan-Sweet, J. *Chem. Mater.* **2006**, *18*, 6278−6282.
(21) Edwards, T. G.; Hung, I.; Gan, Z.; Kalkan, B.; Raoux, S.; Sen, S. *J. Appl. Phys.* **2013**, *114* (21), 233512−7.
(22) Kalkan, B.; Sen, S.; Cho, J.-Y.; Joo, Y.-C.; Clark, S. M. *Appl. Phys. Lett.* **2012**, *101*, 151906−5.
(23) Poole, P. H.; Grande, T.; Angell, C. A.; McMillan, P. F. *Science* **1997**, *275* (5298), 322−323.
(24) Angell, C. A. *Science* **1995**, *267* (5206), 1924−1935.
(25) Sheng, H. W.; Liu, H. Z.; Cheng, Y. Q.; Wen, J.; Lee, P. L.; Luo, W. K.; Shastri, S. D.; Ma, E. *Nat. Mater.* **2007**, *6* (3), 192−197.
(26) Vaccari, M.; Garbarino, G.; Aquilanti, G.; Coulet, M. V.; Trapananti, A.; Pascarelli, S.; Hanfland, M.; Stavrou, E.; Raptis, C. *Phys. Rev. B: Condens. Matter Mater. Phys.* **2010**, *81* (1), 014205−6.
(27) Katayama, Y.; Mizutani, T.; Utsumi, W.; Shimomura, O.; Yamakata, M.; Funakoshi, K. *Nature* **2000**, *403* (6766), 170−173.
(28) Aasland, S.; McMillan, P. F. *Nature* **1994**, *369* (6482), 633−636.
(29) Tanaka, H. *Phys. Rev. E: Stat. Phys., Plasmas, Fluids, Relat. Interdiscip. Top.* **2000**, *62* (5), 6968−6976.
(30) SMART, v. a.-., SAINT, v4, 5, and 6 1994−1999, *SADABS, SHELXTL V-5*; Bruker Analytical Xray Systems Inc.: Madison, WI.
(31) Chupas, P. J.; Qiu, X.; Hanson, J. C.; Lee, P. L.; Grey, C. P.; Billinge, S. J. L. *J. Appl. Crystallogr.* **2003**, *36*, 1342−1347.
(32) Hammersley, A. P.; Svensson, S. O.; Hanfland, M.; Fitch, A. N.; Hausermann, D. *High Pressure Res.* **1996**, *14*, 235−248.
(33) Egami, T.; Billinge, S. J. L. *Pergamon Mater. Ser.* **2003**, *7*, vii.
(34) Qiu, X.; Thompson, J. W.; Billinge, S. J. L. *J. Appl. Crystallogr.* **2004**, *37*, 678.
(35) Proffen, T.; Billinge, S. J. L. *J. Appl. Crystallogr.* **1999**, *32*, 572−575.
(36) McCarthy, T. J.; Ngeyi, S. P.; Liao, J. H.; DeGroot, D. C.; Hogan, T.; Kannewurf, C. R.; Kanatzidis, M. G. *Chem. Mater.* **1993**, *5* (3), 331−340.
(37) Blöchl, P. E. *Phys. Rev. B: Condens. Matter Mater. Phys.* **1994**, *50*, 17953−17979.
(38) Kresse, G.; Furthmuller, J. *Phys. Rev. B: Condens. Matter Mater. Phys.* **1996**, *54* (16), 11169−11186.
(39) Kresse, G.; Hafner, J. *Phys. Rev. B: Condens. Matter Mater. Phys.* **1994**, *49* (20), 14251−14269.
(40) Perdew, J. P.; Burke, K.; Ernzerhof, M. *Phys. Rev. Lett.* **1996**, *77* (18), 3865−3868.
(41) Heyd, J.; Scuseria, G. E.; Ernzerhof, M. *J. Chem. Phys.* **2003**, *118*, 8207−8215.
(42) Heyd, J.; Scuseria, G. E.; Martin, R. L. *J. Chem. Phys.* **2005**, *123*, 174101−08.
(43) Kresse, G.; Hafner, J. *Phys. Rev. B: Condens. Matter Mater. Phys.* **1993**, *47* (1), 558−561.
(44) Hoppe, R. *Angew. Chem., Int. Ed. Engl.* **1970**, *9*, 25−34.
(45) Hoppe, R.; Voigt, S.; Glaum, H.; Kissel, J.; Muller, H.; Bernet, K. *J. Less-Common Met.* **1989**, *156*, 105−122.
(46) Chung, D. Y.; Choi, K. S.; Iordanidis, L.; Schindler, J. L.; Brazis, P. W.; Kannewurf, C. R.; Chen, B. X.; Hu, S. Q.; Uher, C.; Kanatzidis, M. G. *Chem. Mater.* **1997**, *9* (12), 3060−3071.
(47) Mott, N. F.; Davis, E. A. *Electronic Process in Noncrystalline Materials*; Clarendon Press: Oxford, 1979.
(48) Hudgens, S.; Johnson, B. *MRS Bull.* **2004**, *29*, 829−832.
(49) Huang, B.; Robertson, J. *Phys. Rev. B: Condens. Matter Mater. Phys.* **2012**, *85*, 125305.
(50) Lotnyk, A.; Bernütz, S.; Sun, X.; Ross, U.; Ehrhardt, M.; Rauschenbach, B. *Acta Mater.* **2016**, *105*, 1−8.

DOI: 10.1021/jacs.8b05542
J. Am. Chem. Soc. 2018, 140, 9261−9268